

The Global Warming–Induced South Asian High Change and Its Uncertainty

XIA QU

State Key Laboratory of Numerical Modeling for Atmospheric Sciences and Geophysical Fluid Dynamics, Institute of Atmospheric Physics, Chinese Academy of Sciences, Beijing, and Plateau Atmosphere and Environment Key Laboratory of Sichuan Province, Chengdu University of Information and Technology, Chengdu, and Joint Center for Global Change Studies, Beijing, China

GANG HUANG

State Key Laboratory of Numerical Modeling for Atmospheric Sciences and Geophysical Fluid Dynamics, Institute of Atmospheric Physics, Chinese Academy of Sciences, and Joint Center for Global Change Studies, Beijing, China

(Manuscript received 4 September 2015, in final form 30 December 2015)

ABSTRACT

Based on models from phase 5 of the Coupled Model Intercomparison Project (CMIP5), the present study investigates the South Asian high (SAH) change in response to global warming. Under global warming, the selected 16 coupled general circulation models all feature an elevation of geopotential height at 100 hPa to the south of the SAH climatological position; an easterly response is found over the northern Indian Ocean in all the models, while a westerly response is found over subtropical Asia. The ridges of the SAH shift equatorward in 75% of models. Using the linear baroclinic model, it is found that the combined effects of latent heating and the mean advection of stratification change (MASC) are mainly responsible for those responses. The MASC mainly leads to the aforementioned easterly and westerly responses; the latent heating contributes to the geopotential height response and the easterly response over the northern Indian Ocean. The most important intermodel diversity is found in the 100-hPa circulation change under global warming, accounting for more than half of the total intermodel variance. The intermodel spread of latent heating and the MASC are important factors in driving the 100-hPa circulation diversity. Furthermore, analysis shows that the projected uncertainties in humidity, vertical velocity, and global mean temperature change are the three most important sources of intermodel diversity for the 100-hPa circulation change.

1. Introduction

In northern summer, a huge anticyclone exists in the upper troposphere over subtropical Asia (Figs. 1a,e). The anticyclone, called the South Asian high (SAH), forms because of the sensible heat flux of the Tibetan Plateau and South Asian monsoon precipitation (Boos and Kuang 2010; Duan and Wu 2005; Flohn 1960; Hoskins and Rodwell 1995). It is the strongest and steadiest system in the upper troposphere (Li et al. 2005; Mason and Anderson 1963). The subtropical westerly jet on the northern flank of the SAH is an important environmental forcing of the important climatic phenomenon of East Asia, the mei-yu-baiu rainband (Sampe and Xie 2010), which brings the major rainy season to the densely populated region. The

northerly flow to the east of the SAH and the underlying low-level southerly combine to provide the necessary basic flow that forms the tilt structure of the Pacific–Japan pattern (Kosaka and Nakamura 2006).

The SAH modulates the western Pacific subtropical high (Tao and Zhu 1964), which is important for the variability of the East Asian summer monsoon (Huang and Wu 1989; Huang and Sun 1992; Tao and Chen 1987; Wu and Chen 1998) and the emergence of severe floods and droughts in East Asia (Huang et al. 1999). For year-to-year variations, the simulation results of Zhao et al. (2009) show that an intensified SAH leads to a strengthened and southwestwardly located western Pacific subtropical high. Consequently, rainfall over the northwestern Pacific decreases and precipitation over subtropical East Asia increases (Zhang et al. 2005; Zhao et al. 2007). In addition, studies suggest that the interannual variability of the SAH is associated with the South Asian monsoon, the mid-Pacific trough, and the Mexican high (Zhang et al. 2005; Zhao et al. 2007).

Corresponding author address: Dr. G. Huang, P.O. Box 9804, Beijing 100029, China.
E-mail: hg@mail.iap.ac.cn

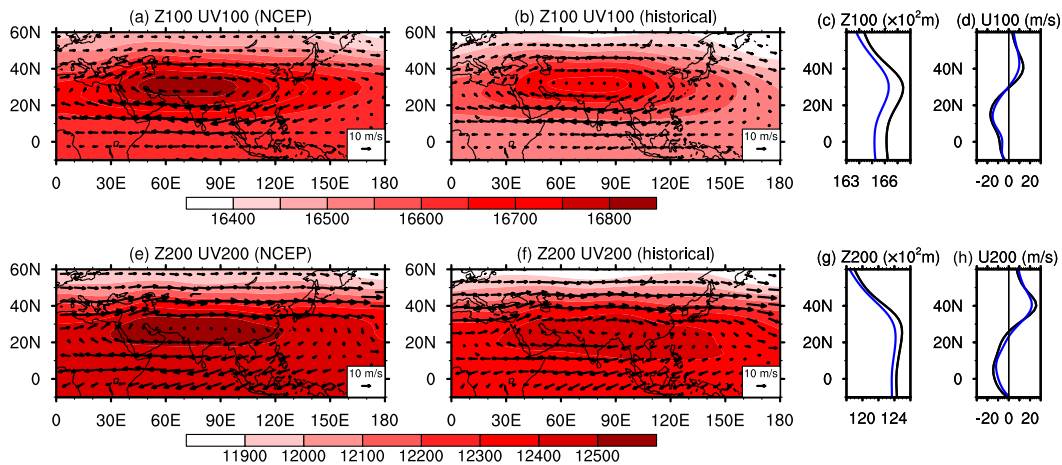


FIG. 1. (a),(b),(e),(f) The climatology of the upper-tropospheric geopotential height (m; color shading) and wind (vectors). Shown are the results of NCEP–NCAR reanalysis in (a),(e) and the MME results of CMIP5 historical runs in (b),(f). (c),(d),(g),(h) The zonal mean of the upper-tropospheric geopotential height and zonal wind for the Eastern Hemisphere over 10°S – 60°N ; note that the results in (c),(g) are geopotential height (m) and the results in (d),(h) are zonal wind (m s^{-1}). Black and blue lines in (c),(d),(g),(h) are the results of NCEP–NCAR reanalysis and the MME of CMIP5 historical runs, respectively. Also, the results for 100 hPa are shown in (a)–(d), and the results for 200 hPa are shown in (e)–(h).

Greenhouse gas concentrations in the atmosphere have been increasing since the Industrial Revolution, contributing to a rise in global surface temperature. Nevertheless, the rise is spatially uneven because of many factors, including the uneven distribution of land surface around the globe (Sutton et al. 2007), the ice and snow albedo feedback (Manabe et al. 1990), and poleward energy transport (Cai 2005). This tends to cause an inhomogeneous response in the atmosphere (Xie et al. 2010), including the SAH (Qu et al. 2015). Using the output from phase 5 of the Coupled Model Intercomparison Project (CMIP5; Meehl et al. 2009), Qu et al. (2015) found that the SAH may shift equatorward in response to global warming, and that the latent heating associated with the precipitation over South Asia and the western Pacific is responsible. The latent heating may cause a remote response in the atmosphere (Chiang and Sobel 2002). The contribution of latent heating outside these regions is unknown. Ma et al. (2012) proposed that besides latent heating, another thermodynamic factor—the mean advection of stratification change (MASC)—exerts a profound influence on the atmospheric response to global warming. Does MASC contribute to the SAH change under global warming? If so, exactly how is the SAH affected by the MASC? Besides, the SAH in fact behaves very differently in individual coupled general circulation models (Qu et al. 2015). It is unknown which dynamic or thermodynamic factor in the models contributes most to the diversity.

The paper is organized as follows: section 2 introduces the data and methods used in the study; section 3 covers the SAH change, as well as the associated circulation change in response to global warming; section 4 studies the mechanism of the SAH change under global warming using a conceptual model; section 5 investigates the intermodel diversity of the SAH change and its sources; and sections 6 and 7 provide the discussion and summary, respectively.

2. Data and method

This investigation is based on CMIP5 outputs. Information about the CMIP5 models is listed in Table 1. The experiments used in this study are historical and representative concentration pathway 4.5 (RCP4.5) scenario simulations. The historical experiments were conducted based on observed anthropogenic and natural forcing from the mid-nineteenth century to about 2005. In the RCP4.5 experiments, the CMIP5 models were forced by gradually increasing radiative forcing, stabilizing at 4.5 W m^{-2} after 2100 (Thomson et al. 2011). For detailed information, readers are referred to <http://cmip-pcmdi.llnl.gov/cmip5/>. The multimodel ensembles (MMEs) of the CMIP5 models are valid for studying the SAH given the reproducibility of the SAH and the associated features (Qu et al. 2015). The geopotential height at each grid is subtracted by global mean geopotential height because 1) the focus of the present study is the pattern response and 2) the upper-tropospheric geopotential height is generally elevated in the warming climate according to the hydrostatic equation.

TABLE 1. Climate model details. (Expansions of acronyms are available online at <http://www.ametsoc.org/PubsAcronymList>.)

Model	Country of origin	Atmospheric resolution (lon \times lat grid points)
CanESM2	Canada	128 \times 64
CNRM-CM5	France	256 \times 128
CSIRO Mk3.6.0	Australia	192 \times 96
FGOALS-s2	China	128 \times 96
GFDL CM3	United States	144 \times 90
GFDL-ESM2G	United States	144 \times 90
GISS-E2-R	United States	144 \times 90
HadGEM2-ES	United Kingdom	192 \times 145
INM-CM4.0	Russia	180 \times 120
IPSL-CM5A-LR	France	96 \times 96
MIROC-ESM	Japan	128 \times 64
MIROC-ESM-CHEM	Japan	128 \times 64
MIROC5	Japan	256 \times 224
MPI-ESM-LR	Germany	192 \times 96
MRI-CGCM3	Japan	320 \times 160
NorESM1-M	Norway	144 \times 96

The model responses to global warming are represented by the difference between the climatology of future (2069–98) and present-day simulations (1975–2004). Only the run “r1i1p1” of each model is analyzed. The MME approach is used to reduce natural variability and systematic biases in the models. The model outputs are interpolated onto a $1.0^\circ \times 1.0^\circ$ grid using a bilinear interpolation technique. The analysis focuses on summer (i.e., the June–August mean). The performance of CMIP5 models are evaluated against the National Centers for Environmental Prediction–National Center for Atmosphere Research (NCEP–NCAR) atmospheric reanalysis with a horizontal resolution of $2.5^\circ \times 2.5^\circ$ (Kalnay et al. 1996).

The linear baroclinic model is used to study the atmospheric response to heating. It is constructed by atmospheric primitive equations and allows examination of linear dynamics in the atmosphere, including a steady linear response to a prescribed forcing, eigenanalysis, and so on. In this study, the component of steady forcing is adopted. The heating forcing is identical to that in the CMIP5 results, except that it is linearly interpolated into the resolution of the linear baroclinic model. The climatology in the linear baroclinic model is the same as the summer mean of the CMIP5 MME in the present-day simulations. The model has a horizontal spectral resolution of T42 and 20 sigma (σ) levels in the vertical. The horizontal diffusion has an e -folding decay time of 6 h for the largest wavenumber. The Rayleigh friction and Newtonian damping have a frequency scale of 0.5 day^{-1} for $\sigma \geq 0.9$ and $\sigma \leq 0.02$ and 30 day^{-1} for $0.02 < \sigma < 0.9$. The vertical diffusion is set at 1000 day^{-1} at all levels. Further details are given in Watanabe and

Kimoto (2000). The response of the linear baroclinic model reaches steady state at day 15, and the 15–20-day mean results are displayed as steady forcing to the prescribed heating source or sink.

3. The SAH in present climate

Before investigate the SAH change under the scenario with higher greenhouse gas concentration, we need to examine how the CMIP5 models generally behave in the SAH. Here, we compared the CMIP5 MME with the NCEP–NCAR reanalysis.

At 100 hPa, the climatological circulation features a huge zonally elongated anticyclone, the SAH (Fig. 1a). The SAH center resides near 30°N , 70° – 80°E (Figs. 1a,c,d). The northern flank is the Asian subtropical westerly jet, with its maximum around 42.5°N (Fig. 1d). The easterly wind is located south of the SAH center, with its maximum around 15°N (Fig. 1d). In the CMIP5 MME results, tiny discrepancies are found in that 1) the geopotential height is slightly lower than the NCEP–NCAR reanalysis (Fig. 1c) and 2) the SAH is meridionally larger, with its westerly (easterly) maximum slightly northward (southward). Despite the small discrepancies, the MME reasonably reproduces the features of the SAH (Figs. 1b–d).

As in the results at 100 hPa, the SAH is the dominant feature at 200 hPa in observations (Fig. 1e). Compared with those at 100 hPa, the SAH is southward: 1) the center is located at 25°N (Figs. 1e,h,i) and 2) the latitude of the maximum westerly (easterly) wind in the north (south) flank is 40°N (5°N) (Figs. 1e,i). The CMIP5 MME also slightly underestimates the geopotential height (Figs. 1e–g). The SAH is meridionally smaller compared with the observation (Figs. 1e,f,i). Although tiny discrepancies exist between simulations and observation, the CMIP5 MME has the capacity of reproducing the SAH at this pressure level.

Compared to the simulation results at the above pressure levels, the CMIP5 MME exhibits almost the same skill for the SAH and is qualified to investigate of the response of the SAH to global warming.

4. The SAH change

Figure 2 displays the zonal wind differences, averaged over 10° – 140°E , between RCP4.5 and historical simulation. Under global warming, the dominant feature of zonal wind change over 10° – 140°E is the easterly change around 0° – 20°N and the westerly change around 30° – 50°N at 100 hPa. Figure 3 displays the circulation differences between the RCP4.5 and historical simulation at 100 hPa. Under global warming, the geopotential height at 100 hPa is elevated over tropical and subtropical

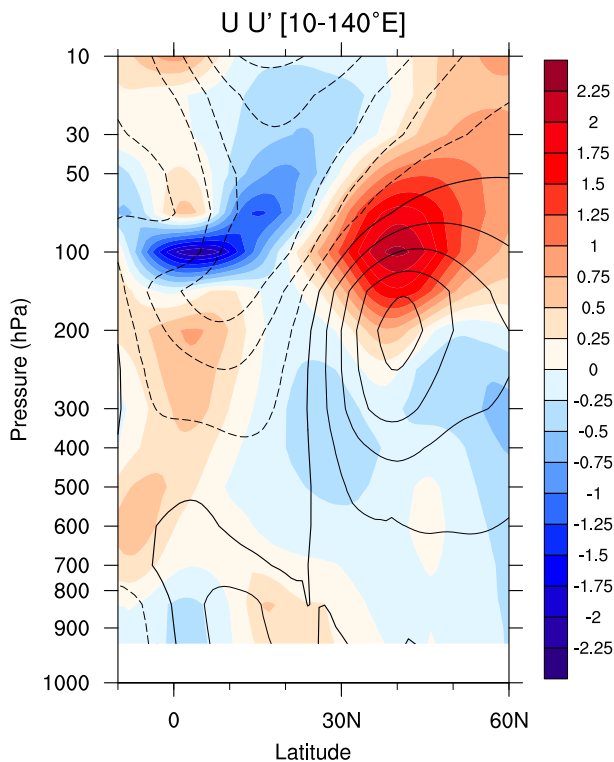


FIG. 2. The zonally averaged climatological zonal wind (contours, interval is 5 m s^{-1}) and the zonally averaged differences of zonal wind between RCP4.5 and historical simulations (m s^{-1} ; shading). All the results are based on the MME results from 10° to 140°E . Dashed contours mean the corresponding zonal wind is easterly.

Asia. The maximum occurs from the South China Sea to the Arabian Peninsula, south of the climatological maximum in the historical simulation (Fig. 1b). An anomalous westerly exists around 30° – 50°N and an anomalous easterly over the northern Indian Ocean. The westerly and easterly responses exceed the 90% significance level. The anomalous zero zonal wind line is about 20°N (Figs. 2 and 3), south of that in the historical simulation (Fig. 1b). The SAH under global warming expands southward at 100 hPa.

The southward expansion of the SAH at 100 hPa is generally projected by the CMIP5 models. Figure 4a displays the latitude differences of the SAH ridges (0 m s^{-1} zonal wind) over 10° – 140°E between RCP4.5 and historical simulations. Among the models, at 100 hPa, 13 models (CanESM2, CNRM-CM5, CSIRO Mk3.6.0, FGOALS-s2, GFDL-ESM2G, GISS-E2-R, HadGEM2-ES, IPSL-CM5A-LR, MIROC-ESM, MIROC-ESM-CHEM, MIROC5, MPI-ESM-LR, and MRI-CGCM3) display an equatorward SAH in response to global warming; three models (GFDL CM3, INM-CM4.0, and NorESM1-M) show poleward movement. Also, the latitude differences of the subtropical jet (maximum zonal wind) to the north over 10° – 140°E between RCP4.5 and historical simulations

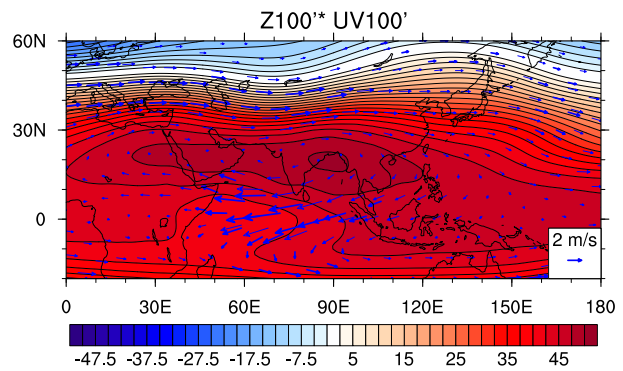


FIG. 3. The differences of geopotential height (m; shading and contours) and wind (vectors) at 100 hPa between RCP4.5 and historical simulations. The wind anomaly at 90% significance level is displayed with thickened vectors. All the results are based on the MME results.

are calculated (Fig. 4b). Among the models, the corresponding southward movement at 100 hPa is less consistent than that of the SAH ridge, with 10 out of 16 models displaying an equatorward shift. Thus, under global warming, the SAH is likely to expand southward at 100 hPa.

The anomalous circulation at 100 hPa is consistent in individual models. Figure 5 displays the geopotential height over South Asia and the zonal wind over midlatitude Asia and the northern Indian Ocean at 100 hPa in response to global warming. Over South Asia, all the CMIP5 models project an elevated geopotential height at 100 hPa; over midlatitude Asia, the zonal wind response in the CMIP5 models is an anomalous westerly; over northern Indian Ocean, the easterlies are all enhanced under global warming.

At 200 hPa, the response to global warming is not significant and is less consistent. Over the equator and northward, the 10° – 140°E averaged zonal wind response is less than 1 m s^{-1} , weaker than that at 100 hPa (Fig. 2). The wind at this pressure level seldom reaches the 90% significance level (figure not shown). Seven models out of 16 do not project an equatorward shift of the SAH ridge (Fig. 4a); five out of the 16 models do not project southward movement of the subtropical jet to the north (Fig. 4b). Thus, the response at 100 hPa is the main focus of present investigation.

5. Mechanism of the SAH change

Heating is one of the most important factors of the atmospheric adjustment (Gill 1980; Matsuno 1966). Here, we study the role of heating on the SAH change. After considering the order of the each term in both tropics and subtropics, as in Ma et al. (2012), the thermodynamic equation of atmospheric temperature change under global warming is simplified into

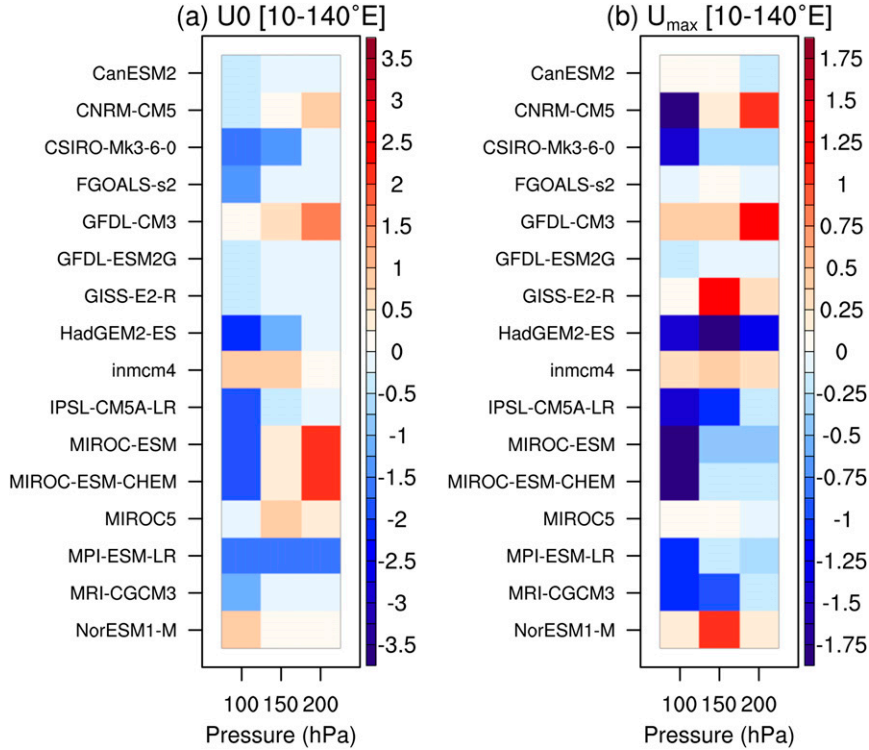


FIG. 4. The latitude change of (a) 0 m s^{-1} zonal wind and (b) maximum zonal wind in the RCP4.5 simulation relative to those in historical simulations at 100, 150, and 200 hPa. The blue-shaded boxes denote the latitude of 0 m s^{-1} zonal wind or maximum zonal wind of the model at the pressure level shifts southward, and red-shaded boxes denote the latitude shifts northward. The results are based on the average of $10^\circ\text{--}140^\circ\text{E}$.

$$B \left(\bar{\omega} \frac{\partial \theta^*}{\partial p} + \omega' \frac{\partial \bar{\theta}}{\partial p} \right) = -B \bar{\omega} \frac{\partial \langle \theta' \rangle}{\partial p} + \text{LH}^* + \text{SH}^* + Q_R^*, \quad (1)$$

where the overbar and prime indicate the climatology in the historical simulation and the difference between RCP4.5 and historical simulation, respectively. Here ω is the pressure velocity, θ is the potential temperature, p is the pressure, $B = (p/p_s)^{R/C_p}$, and $p_s = 1000 \text{ hPa}$; also, R is the gas constant for air, C_p is the specific heat at constant pressure, LH is the latent heating, SH is the sensible heating, and Q_R is the radiation. The global average is denoted as $\langle X \rangle$ and the spatial pattern as $X^* = X' - \langle X' \rangle$.

To estimate LH with height, we represent as the apparent moisture sink (Luo and Yanai 1984). The linearized latent heating change under global warming is written as

$$\text{LH}' = -L \left(\bar{\mathbf{V}} \cdot \nabla q' + \mathbf{V}' \cdot \nabla \bar{q} + \bar{\omega} \frac{\partial q'}{\partial p} + \omega' \frac{\partial \bar{q}}{\partial p} \right). \quad (2)$$

Here L is the latent heat of condensation, \mathbf{V} is the horizontal wind, and q is the specific humidity. The values of

SH and Q_R with height are difficult to estimate. For convenience, we write the residual terms RE as

$$\text{RE} = \text{SH} + Q_R. \quad (3)$$

The RE with height can be estimated. The linearized RE change under global warming is

$$\text{RE}' = Q_1' - \text{LH}'. \quad (4)$$

Here

$$Q_1' = C_p \left(\bar{\mathbf{V}} \cdot \nabla T' + \mathbf{V}' \cdot \nabla \bar{T} + B \bar{\omega} \frac{\partial \theta'}{\partial p} + B \omega' \frac{\partial \bar{\theta}}{\partial p} \right) \quad (5)$$

and T is the temperature. Thus, (1) can be written as

$$B \left(\bar{\omega} \frac{\partial \theta^*}{\partial p} + \omega' \frac{\partial \bar{\theta}}{\partial p} \right) = -B \bar{\omega} \frac{\partial \langle \theta' \rangle}{\partial p} + \text{LH}^* + \text{RE}^*. \quad (6)$$

As $\langle \theta' \rangle$ is the global averaged potential temperature response to global warming, $\partial \langle \theta' \rangle / \partial p$ means the stratification change. Consequently, the first term on the right-hand side of (6) is called the MASC. In this paper, we use

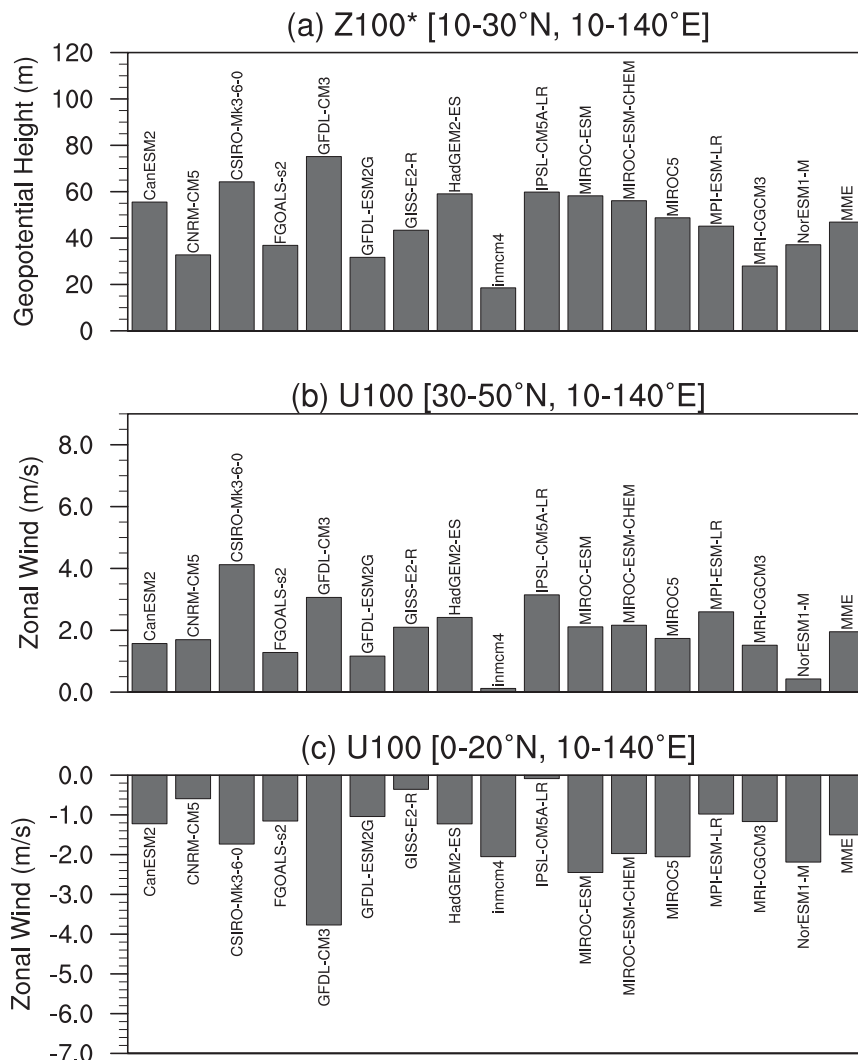


FIG. 5. (a) The area averaged differences of the geopotential height (m) over 10°–30°N, 50°–140°E, and the zonal wind (m s^{-1}) averaged over (b) 30°–50°N, 50°–140°E and (c) 0°–20°N, 50°–140°E at 100 hPa between RCP4.5 and historical simulations.

the three terms on the right-hand side to force the linear baroclinic model to study their influences on the SAH. The forcing is the MME of the forcing calculated in the individual models. No multiplication is performed on the forcing terms when the model is forced.

Figure 6 displays the distribution of the mass integration of the three terms from the surface to the upper troposphere. Under global warming, latent heating is enhanced over the Asian monsoon regions, the northwestern Pacific, the equatorial North Pacific, the equatorial North Atlantic, and tropical North Africa; it generally weakens over the Southern Hemisphere, the tropical North Atlantic, northwest of the Tibetan Plateau, and in North Africa. The latent heating pattern may be due to the combined effects of

humidity and SST change in response to global warming (Huang et al. 2013). The integrated MASC pattern is generally opposite to the latent heating pattern. The MASC is negative over the intertropical convergence zone and is positive over the southern Indian Ocean, the east coast of the subtropical Pacific, and the east coast of the subtropical Atlantic. The pattern is determined by the distribution of climatological vertical velocity since $\langle \theta' \rangle$ is globally uniform. The amplitude is approximately a quarter the amplitude of the latent heating. The residual term is generally small over the tropics. Its amplitude is half the amplitude of the latent heating over the subtropics and midlatitudes. Near the SAH, a positive RE^* is found to the northwest of the Tibetan Plateau.

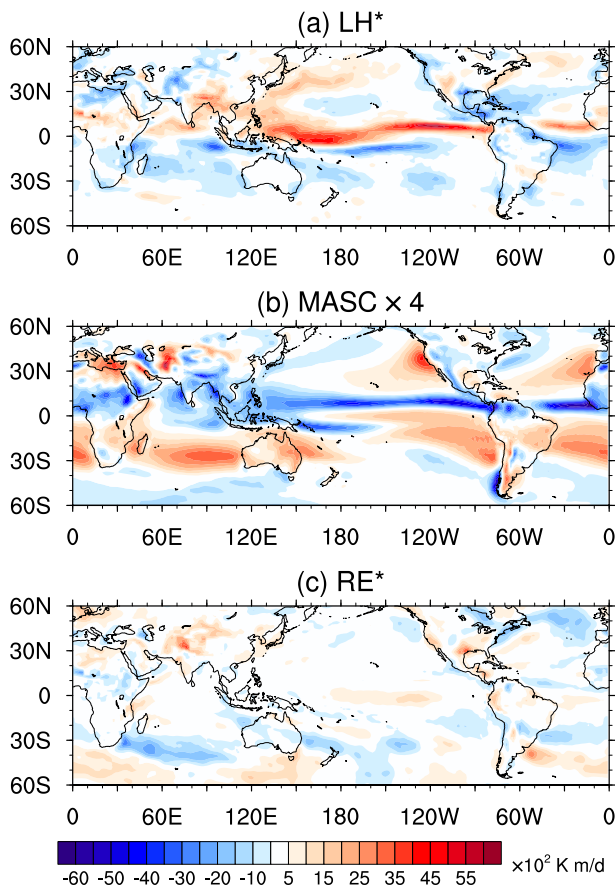


FIG. 6. The distribution of the mass integration of (a) the latent heating change pattern, (b) MASC, and (c) the residual terms change pattern from the surface to 100 hPa (K m day^{-1}). The results of MASC are multiplied by 4 for display clarity.

When the linear baroclinic model is forced by the term LH^* , a positive geopotential height and anticyclone response is generated in the upper troposphere above the Tibetan Plateau; an anomalous easterly exists over 5° – 30°N , and a westerly over 35° – 60°N in the model (Fig. 7a). The amplitude of the linear baroclinic model responses is smaller than that of CMIP5 MME results. It may arise from the inconsistency of the Rayleigh friction and Newtonian damping between the linear baroclinic model and the CMIP5 models. The latitudes of the maximum geopotential height and zero zonal wind both shift northward in the CMIP5 MME results (Figs. 3, 7a, and 8). The spatial correlation coefficient between the LH^* -forced and CMIP5 MME results is 0.54 with the geopotential height and 0.59 with the zonal wind over the domain 0° – 50°N , 10° – 140°E (Figs. 9a,b).

As the linear baroclinic model is forced by the term MASC, in the model, a dipole response resides over the northern Indian Ocean and subtropical Eurasia: this is formed of a negative geopotential height with cyclonic

wind over midlatitude Asia and anticyclonic wind over South Asia (Fig. 7b). The anomalous easterly over the northern Indian Ocean is well captured (Figs. 7b and 8b). The zero zonal wind and maximum westerly anomaly is slightly equatorward relative to the CMIP5 MME results (Figs. 7b and 8b). Since $\langle \theta' \rangle$ peaks at 300 hPa (figure not shown), the MASC from 300 to 100 hPa is reversed in sign compared to that below 300 hPa (Fig. 10). The profile is quite different to that of the latent heating, which peaks in the midtroposphere. It explains why the responses to the latent heating and the MASC are not opposite, even though the vertical integrated pattern is generally opposite. Besides, the reverse sign of the MASC profile explains that the upper-tropospheric responses to the latent heating and MASC are comparable, although the amplitude of the vertical integrated MASC is a quarter of the latent heating amplitude. Over the domain 0° – 50°N , 10° – 140°E , the spatial correlation coefficient between the linear baroclinic model and the CMIP5 MME results is 0.71 for the geopotential height and 0.55 for the zonal wind (Figs. 9a,b).

For the circulation response at 100 hPa to the MASC, the vertical structure of the MASC over subtropical Asia may be responsible. To understand the circulation response in detail, the MASC is divided into two parts: the heating from 1000 to 300 hPa (hereafter HB) and the heating from 250 to 10 hPa (hereafter HA). For most grids, the signs of HB and HA are opposite (Fig. 10). The two kinds of heating are used to force the linear baroclinic model (LBM). The final effect of the MASC in Fig. 7b is the superimposed effects of HB and HA. The HB yields cyclonic wind at 100 hPa, with westerly response mainly over 15° – 30°N and easterly response mainly over 40° – 50°N (Fig. 11a). It is mainly the Rossby wave response to the cooling over the Tibetan Plateau and its south (Figs. 10a–f). As the LBM is forced by HA, the 100-hPa circulation response exhibits a dipole structure over midlatitude and subtropical Eurasia (Fig. 11b). Anticyclonic wind response resides from the Arabian Peninsula to the northwestern Pacific. Surrounding the Tibetan Plateau, as distance of HB to 100 hPa is farther than that of HA, the anomaly excited by HB may depart farther north than that excited by HA. That is, the anticyclone excited by HA is slightly south of the cyclonic response forced by HB. The addition of the HB and HA yields the MASC-forced cyclonic response over midlatitude of central Asia and East Asia (Fig. 7b). Besides, MASC cooling is found over the Mediterranean Sea and western and central Asia (Figs. 10g–j). It locally produces cyclone over 100 hPa (Fig. 11b). Collaborating with the HB, it contributes to the cyclonic response pattern at 100 hPa over Eurasia (Fig. 7b).

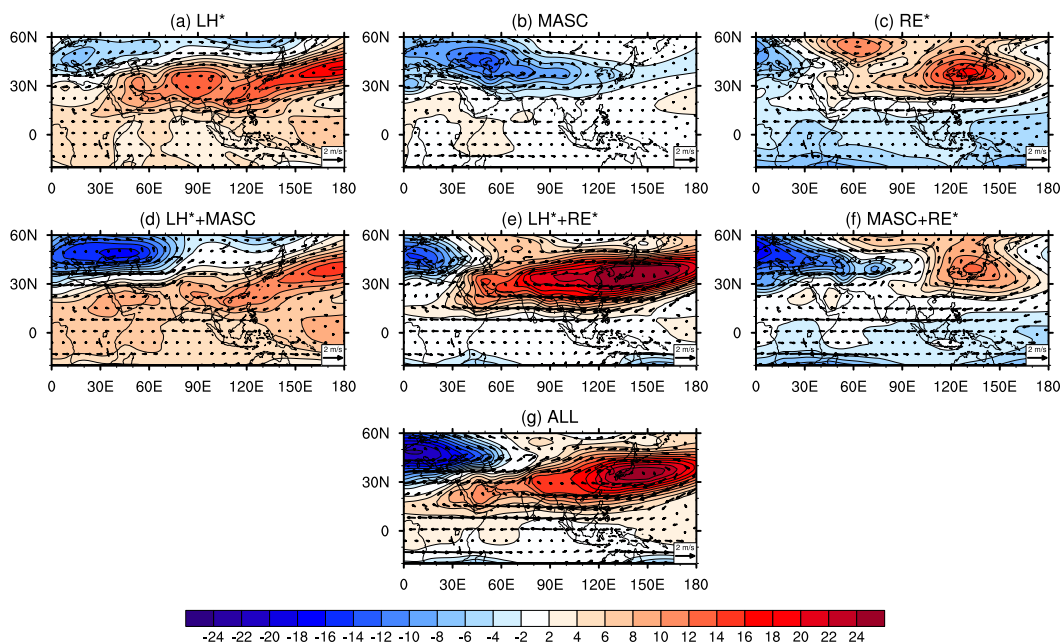


FIG. 7. The response of geopotential height (m; shading and contours) and wind (vectors) at 100 hPa in the linear baroclinic model to (a) LH^* , (b) MASC, and (c) RE^* . Also shown are (d) the sum of (a) and (b), (e) the sum of (a) and (c), (f) the sum of (b) and (d), and (g) the sum of (a), (b), and (c).

In response to the residual terms, anomalous anticyclonic wind is forced in the upper troposphere over East Asia, with a center over the Korea Peninsula and the Sea of Japan in the linear baroclinic model (Fig. 7c). The anomalous anticyclone is farther north than that in the CMIP5 MME (Figs. 3, 7c, and 8a,b). Over the domain 0° – 50° N, 10° – 140° E, the spatial correlation coefficient between the linear baroclinic model and CMIP5 MME results is -0.37 for the geopotential height and 0.54 for the zonal wind (Figs. 9a,b).

The combination of the latent heating and MASC yields a relatively similar spatial pattern of geopotential height and zonal wind at 100 hPa to that of the CMIP5 MME. In the combined result, a prominent anticyclone is located over 0° – 50° N in the Eastern Hemisphere (Fig. 7d). The meridional positions of the geopotential height maximum and zero zonal wind at 100 hPa are well reproduced (Figs. 8a,b). Over the domain 0° – 50° N, 10° – 140° E, the spatial correlation coefficient between the linear baroclinic model and CMIP5 MME results is 0.82 for geopotential height and 0.77 for zonal wind: this is the highest among all the single response and the combined results (Figs. 9a,b). The combination of the latent heating and the residual term forces an anticyclone with a maximum over Japan, north of the anticyclone in the CMIP5 MME (Fig. 7e). The spatial correlation coefficient is 0.06 for geopotential height and 0.58 for zonal wind (Figs. 9a,b). The combination of the MASC and

the residual term forces an anticyclone from northeastern Africa to western India, similar to that in the CMIP5 MME; in addition, an anticyclone exists over Japan (Fig. 7f). The spatial correlation coefficient is 0.20 for geopotential height and 0.71 for zonal wind (Figs. 9a,b). The combined effect of the aforementioned three forcing terms generates a similar pattern to the combination of the latent heating and the residual term (Fig. 7g). The spatial correlation coefficient is 0.41 for geopotential height and 0.73 for zonal wind (Figs. 9a,b).

Generally, the latent heating and MASC promote the similarity of the 100-hPa circulation to the CMIP5 MME, while the residual term reduces it. For the geopotential height at 100 hPa over the domain 0° – 50° N, 10° – 140° E, by comparing MASC with $LH^* + MASC$, RE^* with $LH^* + RE^*$, and MASC + RE^* with $LH^* + MASC + RE^*$, we found that LH^* promotes the spatial correlation coefficients. Similarly, we found that MASC also promotes the spatial correlation coefficients, while the residual term reduces the correlation coefficients (Fig. 9a). For the zonal wind, using a similar comparison, we found that the latent heating and MASC consistently promote the similarity; the residual term reduces the similarity in the cases of LH^* versus $LH^* + RE^*$ and $LH^* + MASC$ versus $LH^* + MASC + RE^*$, while it enhances the similarity in the case of MASC versus MASC + RE^* . Therefore, the latent heating and MASC are two important dynamical

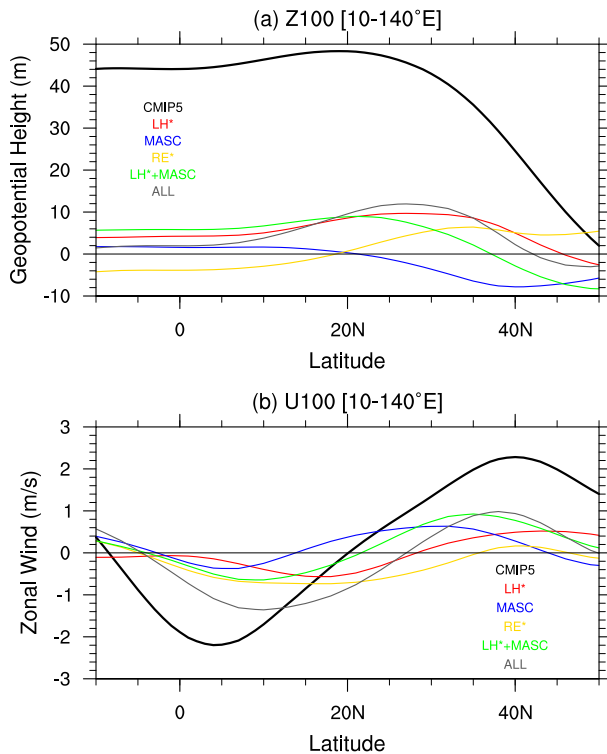


FIG. 8. The zonal average (10° – 140° E) of (a) geopotential height and (b) zonal wind at 100 hPa. The black line is the MME difference between the RCP4.5 and historical simulations. Colored lines are the linear baroclinic model responses: red is LH*, blue is MASC, yellow is RE*, green is LH* + MASC, and gray is LH* + MASC + RE*.

factors in the formation of a global warming–induced SAH change pattern.

6. Uncertainty of the SAH change

Despite the consistency in qualitative projection of the SAH change, intermodel discrepancy exists in the wind and geopotential height (Fig. 5). To reasonably obtain the intermodel spread of the associated circulation, an intermodel empirical orthogonal function (EOF) analysis is performed on the combined field of the projected geopotential height, zonal wind, and meridional wind at 100 hPa over the domain 10° S– 60° N, 10° – 140° E. The geopotential height, zonal wind, and meridional wind are respectively normalized by their intermodel standard deviation at each grid before the EOF analysis is carried out. The leading EOF accounts for 53.7% of the total variance. The normalized first principal component is displayed in Fig. 12b; the regression of the geopotential height and zonal wind at 100 hPa against the normalized principal component is displayed in Fig. 12a.

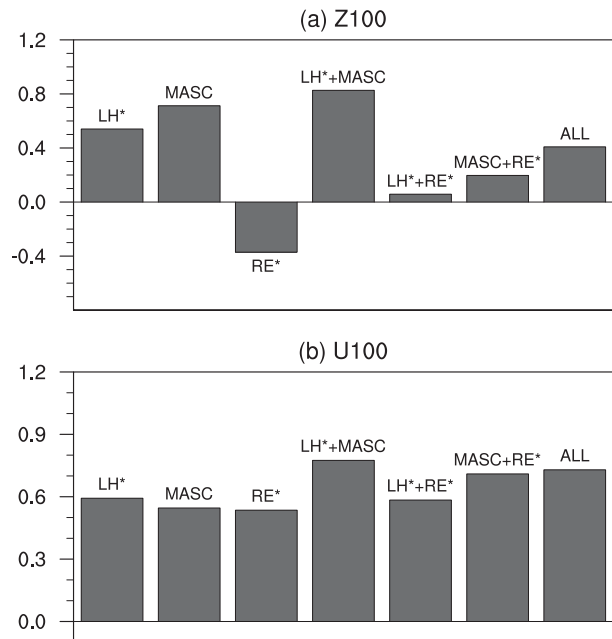


FIG. 9. The spatial correlation of the linear baroclinic model results with the CMIP5 MME results over the domain 0° – 50° N, 10° – 140° E for (a) geopotential height and (b) zonal wind at 100 hPa. ALL is the spatial correlation of the result of sum of LH*, MASC, and RE* with the CMIP5 MME results over the aforementioned domain. The y axis is the correlation coefficient.

Interestingly, the most prominent intermodel diversity of the projected circulation change at 100 hPa is similar to the CMIP5 MME results (Fig. 12a). It also features significant positive geopotential height over the tropics, with its maximum near 10° N. The associated wind anomaly displays a Gill-like pattern, with one anticyclone over the Indian Ocean, South Asia, and the South China Sea, and the other over the southeastern Indian Ocean. The northern anticyclone is larger, implying that the underlying heat source mainly resides to the north of the equator.

Figures 13c–e display the regression of the latent heating, MASC, and the residual terms against the normalized principal component. For latent heating, the intermodel diversity may be associated with the heat sources over the northern Indian Ocean, the western Pacific, north of the equatorial eastern Pacific, the northern Pacific, and the western Tibetan Plateau, and the heat sinks over the southeastern tropical Indian Ocean, the southwestern Indian Ocean, and the northwestern Pacific. Over the Indian Ocean and the western Pacific region, the dipole structure of the latent heating is mainly responsible for the anticyclone response. For MASC, the areas associated the intermodel diversity are wider. The areas with strong climatological ascending and descending motions are linked to the

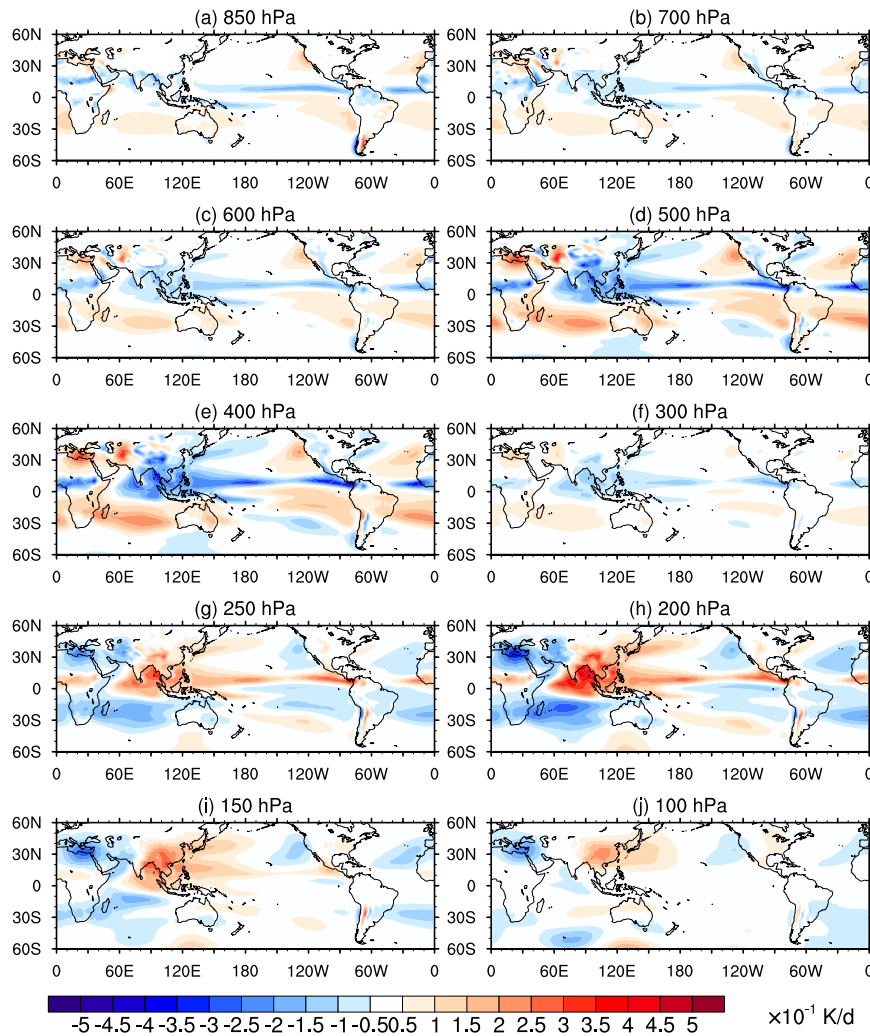


FIG. 10. The MASC at each pressure level. Results at 1000 and 925 hPa are not displayed as data are not available at those levels.

aforementioned intermodel diversity. The vertical profile of the regressed $\langle \theta' \rangle$ is similar to that of the CMIP5 MME; the regressed results reach the 90% significance level at all the pressure levels in the troposphere (figure not shown). For residual terms, the areas with significant linkage to the intermodel spread are scattered. For the patterns of the forcing terms, the amplitudes are similar to the CMIP5 MME results (Fig. 6). For instance, the amplitude of the mass integrated latent heating is approximately 4 times the amplitude of the MASC. Similarly, based on the linear baroclinic model results in section 4, we can conclude that the latent heating and the MASC mainly contribute to the intermodel diversity of the projected circulation change at 100 hPa.

For latent heating regression, the projected vertical velocity and humidity are mainly responsible, while the

contribution of the horizontal wind is weak. Figure 13 displays the regression of the vertical gradient of climatological humidity transported by vertical velocity change, $-\int[(\omega' \partial \bar{q} / \partial p) L / (g C_p)] dp$, and the vertical gradient of humidity change transported by climatological vertical velocity, $-\int[(\bar{\omega} \partial q' / \partial p) L / (g C_p)] dp$, against the normalized principal component. The mass integration is from the surface to 100 hPa. The horizontal advection terms are also computed. The results are not shown as their scale is small compared with the vertical advection terms. The vertical velocity change leads to dipole latent heating anomalies over the Indian Ocean and western Pacific, as well as the heat source over the northwestern Pacific and heat sink over the mid-latitude northern Pacific. For the anomalies over the Indian Ocean and the western Pacific, the SST–wind–rainfall feedback is important for its sustainment (Qu

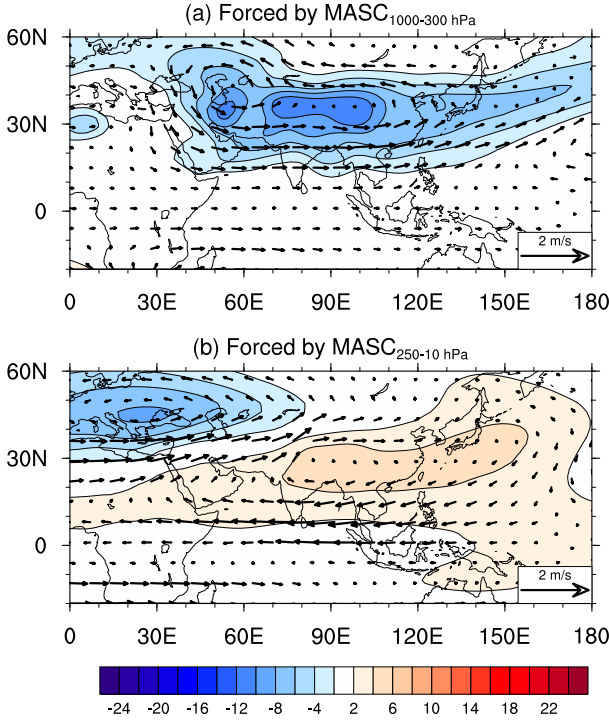


FIG. 11. The response of geopotential height (m; shading and contours) and wind (vectors) at 100 hPa in the linear baroclinic model to MASC (a) from 1000 to 300 hPa and (b) from 250 to 10 hPa.

et al. 2015). The humidity response to global warming results in a quasi-symmetric heat source about the Indo-Pacific equator. The heat sink dominates over the extratropics. The pattern is determined by climatological vertical velocity, similar to the “wet get wetter” mechanism (Chou and Neelin 2004; Held and Soden 2006).

To further investigate the effect of the intermodel diversity of climatology or change to the spread of the 100-hPa circulation change, we defined the MME as X_a and the regression of intermodel diversity against the aforementioned normalized leading principal component as X_d . Based on this analysis, $\omega'_d \partial \bar{q}'_d / \partial p$ is far larger than $\omega'_a \partial \bar{q}'_d / \partial p$ and $\omega'_d \partial \bar{q}'_d / \partial p$, and $\bar{\omega}_a \partial q'_d / \partial p$ is larger than $\bar{\omega}_d \partial q'_d / \partial p$ and $\bar{\omega}_d \partial q'_d / \partial p$. We can therefore derive the following:

$$-\int [(\omega'_d \partial \bar{q}'_d / \partial p) / g]_d dp = -\int [(\omega'_a \partial \bar{q}'_d / \partial p) / g] dp \quad (7)$$

and

$$-\int [(\bar{\omega}_d \partial q'_d / \partial p) / g]_d dp = -\int [(\bar{\omega}_a \partial q'_d / \partial p) / g] dp. \quad (8)$$

Additionally, $\bar{\omega}_d \partial \langle \theta' \rangle'_d / \partial p$ is much smaller than $\bar{\omega}_d \partial \langle \theta' \rangle'_d / \partial p$ and $\bar{\omega}_a \partial \langle \theta' \rangle'_d / \partial p$, so

$$\begin{aligned} -\int [(\bar{\omega}_d \partial \langle \theta' \rangle'_d / \partial p) / g]_d dp &= -\int [(\bar{\omega}_d \partial \langle \theta' \rangle'_d / \partial p) / g] dp \\ &= -\int [(\bar{\omega}_a \partial \langle \theta' \rangle'_d / \partial p) / g] dp. \end{aligned} \quad (9)$$

Here the mass integration is from the surface to 100 hPa. The terms of the right-hand sides of (7), (8), and (9) are displayed in Fig. 14. For the vertical gradient of humidity change, transported by the mean vertical velocity $-\int [(\bar{\omega}_d \partial q'_d / \partial p) / g] dp$, the intermodel spread is mainly caused by the diversity of the humidity change in individual models (Fig. 14a). For the vertical gradient of mean humidity, transported by anomalous vertical velocity $-\int [(\omega'_d \partial \bar{q}'_d / \partial p) / g] dp$, the intermodel spread is mainly caused by the diversity of global warming-induced vertical velocity change in individual models (Fig. 14b). For the forcing MASC diversity, the main contribution is the difference of global mean temperature change between the models (Fig. 14c). In addition, the interaction of the diversity of global warming-induced vertical velocity change and the difference of global mean temperature change contributes part of the MASC diversity (Fig. 14d).

7. Discussion

Qu et al. (2015) pointed out that the precipitation–wind–SST feedback over South Asia, the Indian Ocean, and the western Pacific contributes to the SAH southward. Among the feedback, the latent heating associated with the precipitation response is the key factor. In the present study, results show that the global latent heating change in response to global warming may not lead to the SAH southward. This implies that under global warming the latent heating change over the regions out of South Asia, the Indian Ocean, and the western Pacific may lead to a northward shift of the SAH. Furthermore, the present investigation reveals that the global MASC under global warming plays an important role in the SAH equatorward shift, which is a new result.

Figure 15 displays the regression of the projected and climatological 850-hPa humidity, 500-hPa pressure velocity, and surface temperature against the normalized leading principal component. The projected low-level humidity change associated with the aforementioned leading intermodel diversity mode is significant over most of the globe (Fig. 15a). Following the Clausius–Clapeyron equation, its pattern is approximately determined by climatological surface temperature and the change of surface temperature (Fig. 15e). One may find

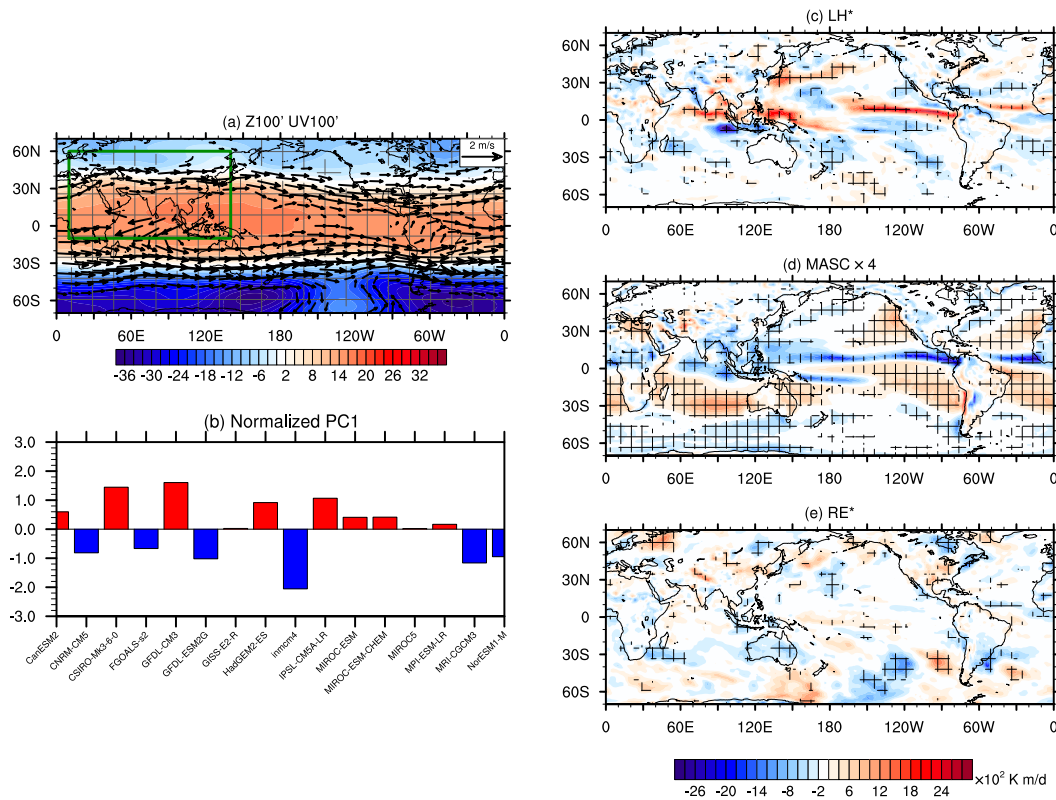


FIG. 12. (a) The regression of the geopotential height (m; shading) and zonal wind (vectors) at 100 hPa, (c) the latent heating change pattern, (d) MASC, and (e) residual terms change pattern against (b) the normalized leading principal component, which is obtained from the intermodel EOF analysis of the combined field of normalized geopotential height and zonal wind at 100 hPa over the domain 10°S – 60°N , 10° – 140°E , shown by the green rectangle in (a). The results in (c)–(e) are the mass integration from the surface to 100 hPa (K m day^{-1}). Lattice hatching indicates the results reaching the 90% significance level. Only vectors at the 90% significance level are shown in (a). The results of MASC in (d) are multiplied by 4 for clarity.

that the diversity of the projected humidity change is comparable at the equator and the northern subtropics, while the surface temperatures over the two regions are not. This may arise from the higher climatological temperature at the equator. The climatological humidity diversity in the models is not related to the leading intermodel diversity mode (Fig. 15b).

The projected change of the midtroposphere velocity associated with the leading intermodel diversity mode generally features descending motion over the tropical southeastern Indian Ocean and the northwestern Pacific, and ascending motion over the northern eastern Pacific and the northern subtropical Pacific (Fig. 15c). The descending motion generally resides over slowly warming oceans, while ascending motion resides over quickly warming oceans (Fig. 15e). The humidity change diversity may cause the spatially uneven rainfall change, leading to the inhomogeneous vertical velocity change. The diversity of the climatological vertical motion is ascent over the

central eastern Indian Ocean and descent over the southwestern Indian Ocean and the southern Indian Ocean (Fig. 15d). The significant cooling associated the leading intermodel diversity mode may favor the structure of the vertical motion over the Indian Ocean (Fig. 15f). To thoroughly separate the influences of the SST change pattern and global mean change of SST on the vertical velocity change, experiments in which the coupled general circulation model is driven by SST with and without patterns are needed.

8. Summary

Using 16 CMIP5 models, we found that the SAH is likely to shift equatorward under global warming: 75% of the selected models project the shift. In all the CMIP5 models, the following features are consistently projected compared with the present climate: 1) the elevation of the 100-hPa geopotential height over tropical and subtropical Asia, 2) an anomalous westerly around

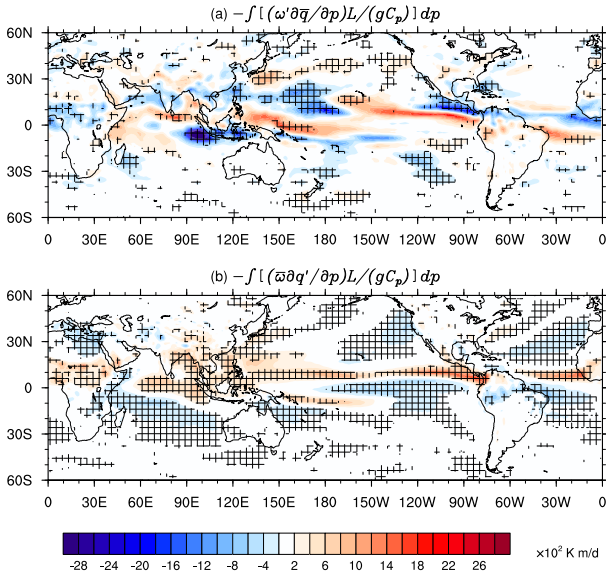


FIG. 13. The regression of (a) the vertical gradient of mean humidity, transported by anomalous vertical velocity, and (b) the vertical gradient of humidity change, transported by the mean vertical velocity, against the normalized leading principal component. The mass integration is from the surface to 100 hPa (K m day^{-1}). Lattice hatching indicates the results reaching 90% significance level.

30°–50°N, and 3) an anomalous easterly over the northern Indian Ocean.

Following Ma et al. (2012), we simplified the forcing of thermodynamic equation of the atmosphere temperature under global warming into three terms: the latent heating, the MASC, and the residual terms. We use the three terms to force the linear baroclinic model and found that the latent heating and the MASC are key to forming the pattern of global warming–induced atmospheric circulation change at 100 hPa over the Asian continent and the Indian Ocean: latent heating yields an intensified SAH, while the MASC shifts the SAH southward. The two terms drive the pattern of the 100-hPa circulation response, similar to that of the CMIP5 MME. However, the residual term generally disfavors the similarity of the forced pattern to the CMIP5 MME.

An intermodel EOF analysis reveals that the most prominent uncertainty pattern of the SAH change in response to global warming is similar to the CMIP5 MME results. It accounts for 53.7% of the total variance. Similar to the CMIP5 MME results, the uncertainties of the latent heating and the MASC are key to the uncertainty of the SAH change. The intermodel diversity of the latent heating mainly arises from the intermodel spread of the projected vertical velocity and humidity. Furthermore, we divide the variables in the CMIP5 models into two parts: the model average and the

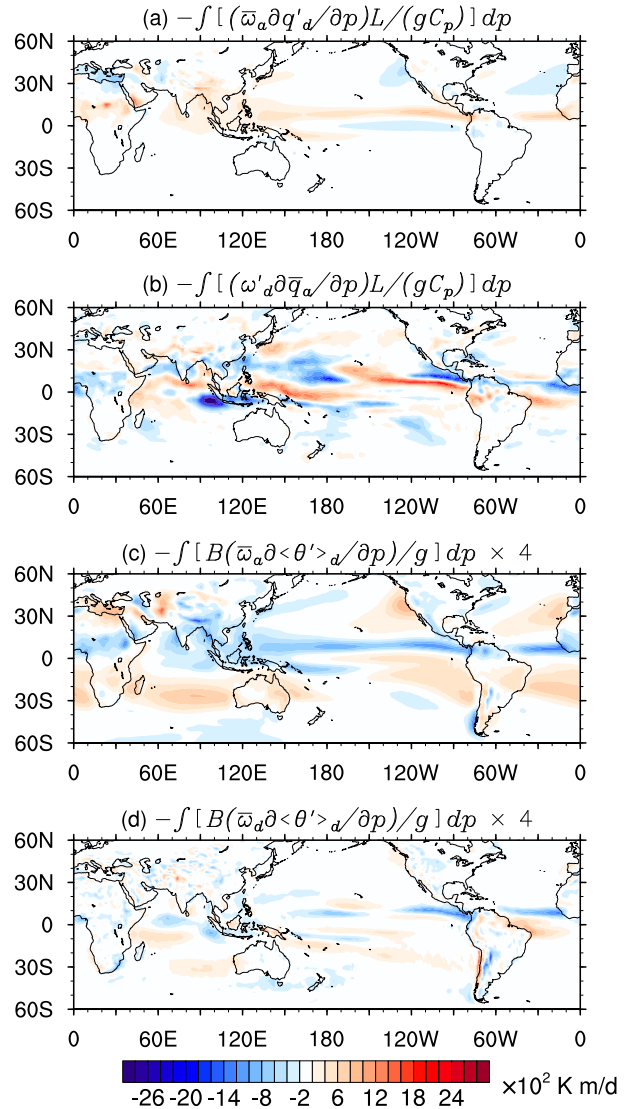


FIG. 14. The distribution of (a) $-\int [(\bar{\omega}_d \partial q'_d / \partial p) L / (g C_p)] dp$, (b) $-\int [(\omega'_d \partial \bar{q} / \partial p) L / (g C_p)] dp$, (c) $-\int [B(\bar{\omega}_d \partial \langle \theta' \rangle_d / \partial p) / g] dp$, and (d) $-\int [B(\bar{\omega}_d \partial \langle \theta' \rangle_d / \partial p) / g] dp$ (K m day^{-1}). The results in (c) and (d) are multiplied by 4 for clarity.

diversity between models. The most prominent uncertainty pattern of the global warming–induced SAH change comes from the model diversity in projected humidity, vertical velocity, and global mean temperature change.

Acknowledgments. We acknowledge the World Climate Research Programme’s Working Group on Coupled Modelling, responsible for CMIP, and we thank the climate modeling groups (listed in Table 1 of this paper) for producing and making available their model output. For CMIP the U.S. Department of Energy’s Program for Climate Model Diagnosis and Intercomparison provides

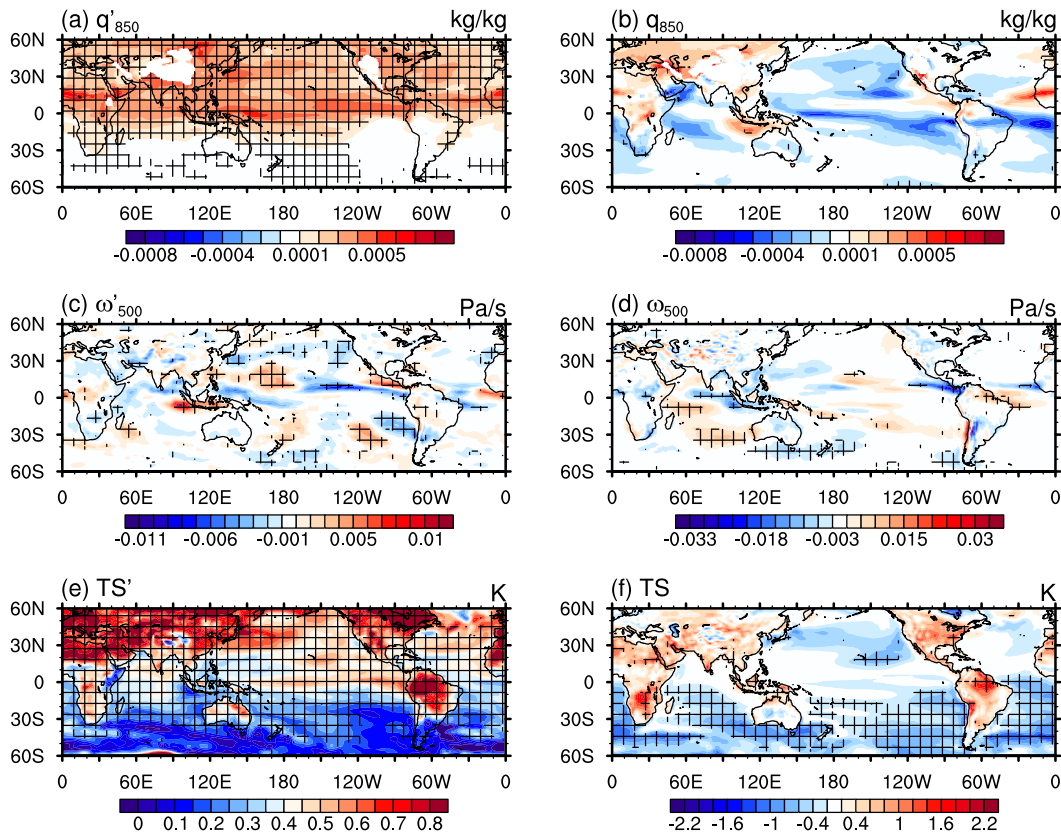


FIG. 15. The regression of (a),(b) 850-hPa humidity (kg kg^{-1}), (c),(d) 500-hPa pressure velocity (Pa s^{-1}), and (e),(f) surface temperature (K) against the normalized leading principal component. In (a),(c), and (e) are the difference between RCP4.5 and historical simulations, and (b),(d), and (f) show the historical simulation. Lattice hatching indicates the results reaching 90% significance level.

coordinating support and led development of software infrastructure in partnership with the Global Organization for Earth System Science Portals. The study was supported by the National Basic Research Program of China (Grant 2012CB955604), National Natural Sciences Foundation of China (Grants 41205050 and 41275083), and Open Research Fund Program of Plateau Atmosphere and Environment Key Laboratory of Sichuan Province (Grant PAEKL-2016-K1).

REFERENCES

- Boos, W. R., and Z. Kuang, 2010: Dominant control of the South Asian monsoon by orographic insulation versus plateau heating. *Nature*, **463**, 218–222, doi:10.1038/nature08707.
- Cai, M., 2005: Dynamical amplification of polar warming. *Geophys. Res. Lett.*, **32**, L22710, doi:10.1029/2005GL024481.
- Chiang, J. C. H., and A. H. Sobel, 2002: Tropical tropospheric temperature variations caused by ENSO and their influence on the remote tropical climate. *J. Climate*, **15**, 2616–2631, doi:10.1175/1520-0442(2002)015<2616:TTVCB>2.0.CO;2.
- Chou, C., and J. D. Neelin, 2004: Mechanisms of global warming impacts on regional tropical precipitation. *J. Climate*, **17**, 2688–2701, doi:10.1175/1520-0442(2004)017<2688:MOGWIO>2.0.CO;2.
- Duan, A. M., and G. X. Wu, 2005: Role of the Tibetan Plateau thermal forcing in the summer climate patterns over subtropical Asia. *Climate Dyn.*, **24**, 793–807, doi:10.1007/s00382-004-0488-8.
- Flohn, H., 1960: Recent investigations on the mechanism of the “summer monsoon” of southern and eastern Asia. *Symposium on Monsoons of the World*, Hind Union Press, 75–88.
- Gill, A. E., 1980: Some simple solutions for heat-induced tropical circulation. *Quart. J. Roy. Meteor. Soc.*, **106**, 447–462, doi:10.1002/qj.49710644905.
- Held, I. M., and B. J. Soden, 2006: Robust responses of the hydrological cycle to global warming. *J. Climate*, **19**, 5686–5699, doi:10.1175/JCLI3990.1.
- Hoskins, B. J., and M. J. Rodwell, 1995: A model of the Asian summer monsoon. Part I: The global scale. *J. Atmos. Sci.*, **52**, 1329–1340, doi:10.1175/1520-0469(1995)052<1329:AMOTAS>2.0.CO;2.
- Huang, P., S.-P. Xie, K. Hu, G. Huang, and R. Huang, 2013: Patterns of the seasonal response of tropical rainfall to global warming. *Nat. Geosci.*, **6**, 357–361, doi:10.1038/ngeo1792.
- Huang, R., and Y. Wu, 1989: The influence of ENSO on the summer climate change in China and its mechanism. *Adv. Atmos. Sci.*, **6**, 21–32, doi:10.1007/BF02656915.
- , and F. Sun, 1992: Impact of the tropical western Pacific on the East Asian summer monsoon. *J. Meteor. Soc. Japan*, **70**, 243–256.
- , G. Huang, and B. Ren, 1999: Advances and problems needed for further investigation in the studies of the East Asian summer monsoon. *Chin. J. Atmos. Sci.*, **23**, 129–141.

- Kalnay, E., and Coauthors, 1996: The NCEP/NCAR 40-Year Reanalysis Project. *Bull. Amer. Meteor. Soc.*, **77**, 437–471, doi:[10.1175/1520-0477\(1996\)077<0437:TNYRP>2.0.CO;2](https://doi.org/10.1175/1520-0477(1996)077<0437:TNYRP>2.0.CO;2).
- Kosaka, Y., and H. Nakamura, 2006: Structure and dynamics of the summertime Pacific–Japan (PJ) teleconnection pattern. *Quart. J. Roy. Meteor. Soc.*, **132**, 2009–2030, doi:[10.1256/qj.05.204](https://doi.org/10.1256/qj.05.204).
- Li, Q., and Coauthors, 2005: Convective outflow of South Asian pollution: A global CTM simulation compared with EOS MLS observations. *Geophys. Res. Lett.*, **32**, L14826, doi:[10.1029/2005GL022762](https://doi.org/10.1029/2005GL022762).
- Luo, H., and M. Yanai, 1984: The large-scale circulation and heat sources over the Tibetan Plateau and surrounding areas during the early summer of 1979. Part II: Heat and moisture budgets. *Mon. Wea. Rev.*, **112**, 966–989, doi:[10.1175/1520-0493\(1984\)112<0966:TLSCAH>2.0.CO;2](https://doi.org/10.1175/1520-0493(1984)112<0966:TLSCAH>2.0.CO;2).
- Ma, J., S. P. Xie, and Y. Kosaka, 2012: Mechanisms for tropical tropospheric circulation change in response to global warming. *J. Climate*, **25**, 2979–2994, doi:[10.1175/JCLI-D-11-00048.1](https://doi.org/10.1175/JCLI-D-11-00048.1).
- Manabe, S., K. Bryan, and M. J. Spelman, 1990: Transient response of a global ocean–atmosphere model to a doubling of atmospheric carbon dioxide. *J. Phys. Oceanogr.*, **20**, 722–749, doi:[10.1175/1520-0485\(1990\)020<0722:TROAGO>2.0.CO;2](https://doi.org/10.1175/1520-0485(1990)020<0722:TROAGO>2.0.CO;2).
- Mason, R. B., and C. E. Anderson, 1963: The development and decay of the 100-mb summertime anticyclone over southern Asia. *Mon. Wea. Rev.*, **91**, 3–12, doi:[10.1175/1520-0493\(1963\)091<0003:TDADOT>2.3.CO;2](https://doi.org/10.1175/1520-0493(1963)091<0003:TDADOT>2.3.CO;2).
- Matsuno, T., 1966: Quasi-geostrophic motions in the equatorial area. *J. Meteor. Soc. Japan*, **44**, 25–43.
- Meehl, G. A., and Coauthors, 2009: Decadal prediction: Can it be skillful? *Bull. Amer. Meteor. Soc.*, **90**, 1467–1485, doi:[10.1175/2009BAMS2778.1](https://doi.org/10.1175/2009BAMS2778.1).
- Qu, X., G. Huang, K. Hu, S.-P. Xie, Y. Du, X.-T. Zheng, and L. Liu, 2015: Equatorward shift of the South Asian high in response to anthropogenic forcing. *Theor. Appl. Climatol.*, **119**, 113–122, doi:[10.1007/s00704-014-1095-1](https://doi.org/10.1007/s00704-014-1095-1).
- Sampe, T., and S.-P. Xie, 2010: Large-scale dynamics of the meiyu–baiu rainband: Environmental forcing by the westerly jet. *J. Climate*, **23**, 113–134, doi:[10.1175/2009JCLI3128.1](https://doi.org/10.1175/2009JCLI3128.1).
- Sutton, R. T., B. Dong, and J. M. Gregory, 2007: Land/sea warming ratio in response to climate change: IPCC AR4 model results and comparison with observations. *Geophys. Res. Lett.*, **34**, L02701, doi:[10.1029/2006GL028164](https://doi.org/10.1029/2006GL028164).
- Tao, S., and F. Zhu, 1964: The variation of 100-mb circulation over South Asia in summer and its association with march and withdrawal of the west Pacific subtropical high. *Acta Meteor. Sin.*, **34**, 385–395.
- , and L. X. Chen, 1987: A review of recent research on the East Asian summer monsoon in China. *Monsoon Meteorology*, C. P. Chang and T. N. Krishnamurti, Eds., Oxford University Press, 60–92.
- Thomson, A. M., and Coauthors, 2011: RCP4.5: A pathway for stabilization of radiative forcing by 2100. *Climatic Change*, **109**, 77–94, doi:[10.1007/s10584-011-0151-4](https://doi.org/10.1007/s10584-011-0151-4).
- Watanabe, M., and M. Kimoto, 2000: Atmosphere–ocean thermal coupling in the North Atlantic: A positive feedback. *Quart. J. Roy. Meteor. Soc.*, **126**, 3343–3369, doi:[10.1002/qj.49712657017](https://doi.org/10.1002/qj.49712657017).
- Wu, R., and L. Chen, 1998: Decadal variation of summer rainfall in the Yangtze–Huaihe River valley and its relationship to atmospheric circulation anomalies over East Asia and the western North Pacific. *Adv. Atmos. Sci.*, **15**, 510–522, doi:[10.1007/s00376-998-0028-2](https://doi.org/10.1007/s00376-998-0028-2).
- Xie, S.-P., C. Deser, G. A. Vecchi, J. Ma, H. Teng, and A. T. Wittenberg, 2010: Global warming pattern formation: Sea surface temperature and rainfall. *J. Climate*, **23**, 966–986, doi:[10.1175/2009JCLI3329.1](https://doi.org/10.1175/2009JCLI3329.1).
- Zhang, P., S. Yang, and V. E. Kousky, 2005: South Asian high and Asian–Pacific–American climate teleconnection. *Adv. Atmos. Sci.*, **22**, 915–923, doi:[10.1007/BF02918690](https://doi.org/10.1007/BF02918690).
- Zhao, P., Y. Zhu, and R. Zhang, 2007: An Asian-Pacific teleconnection in summer tropospheric temperature and associated Asian climate variability. *Climate Dyn.*, **29**, 293–303, doi:[10.1007/s00382-007-0236-y](https://doi.org/10.1007/s00382-007-0236-y).
- , X. Zhang, Y. Li, and J. Chen, 2009: Remotely modulated tropical North Pacific ocean–atmosphere interactions by the South Asian high. *Atmos. Res.*, **94**, 45–60, doi:[10.1016/j.atmosres.2009.01.018](https://doi.org/10.1016/j.atmosres.2009.01.018).